Multiplateau structure caused by spectral interference in high-order harmonic generation from disordered Su-Schrieffer-Heeger chains

Jia-Xiang Chen and Xue-Bin Bian*

Wuhan Institute of Physics and Mathematics, Innovation Academy for Precision Measurement Science and Technology, Chinese Academy of Sciences, Wuhan 430071, China

(Received 3 December 2023; accepted 22 February 2024; published 6 March 2024)

The multiple-plateau structure is a characteristic of high-order harmonic spectra in solids, resulting from strong interband couplings involving three or more bands. Here we show that high-order harmonic generation (HHG) in a two-band Su-Schrieffer-Heeger (SSH) system also exhibits a multiple-plateau structure under disorder effect. For weak external driving fields, the harmonic spectrum of disordered SSH chains exhibits an additional plateau and has a higher cutoff frequency compared with that of ordered SSH chains. The phase analysis of the harmonic spectra from various disordered SSH chains reveals that the second HHG plateau emerges from the interference between different regions. Through time-frequency analysis, we show that the harmonic phase corresponding to the caustic point is more localized than its neighboring orders.

DOI: 10.1103/PhysRevA.109.033104

I. INTRODUCTION

High-order harmonic generation (HHG) is an important tool for creating ultrashort laser pulses [1–3] which can be induced in various systems, including gases [4,5] and crystalline solids [6,7], through nonlinear laser-matter interactions. Similar to the HHG process in gases [8,9], the HHG process in crystals can be described by a three-step model [10–15]: creation, acceleration, and recombination of electron-hole pairs. The acceleration of electron-hole pairs carries the information about the band dispersion of the target material, enabling the use of HHG for the all-optical reconstruction of the electronic band structures [16–18] and berry curvatures [19,20]. Recently, the observation of high-order harmonics from fused silica has suggested that long-range order is not a prerequisite for coherent extreme ultraviolet source generation [21]. The HHG spectra of fused silica and crystalline quartz show similar cutoff energies for the same driving field parameters. Subsequently, HHG in liquids further reveals the roles of short- and long-range correlations in the HHG process [22–26]. The prediction of driving-wavelength-independent cutoff energy by the statistical finite-coherence-distance model [23] was confirmed recently in Ref. [24].

In the process of solving the well-known semiconductor Bloch equations, the weak disorder in the crystals induced by temperature-dependent lattice vibrations is introduced into the theoretical calculations as part of the dephasing time to obtain a high harmonic spectrum with clean peaks [10,27]. However, when the periodicity of the system is broken and long-range order is absent, Bloch states can no longer be used as a basis. In this case, there are two methods to achieve numerical convergence in simulations for disordered systems. One is to consider a sufficiently large system, and the other is the coherent superposition of an adequate number of smaller systems (subsystems) [24,28]. The authors of Ref. [28] demonstrated that HHG spectra obtained by both methods have the same structure, and calculations using the second method converged more rapidly. Disorder in the system causes different phases of radiation harmonics emitted in different regions. Based on the second method, the coherent interference between HHG spectra emitted in different regions of a large system can be understood as the coherent interference of HHG spectra from different subsystems. Thus, apart from generating harmonic spectra with clean odd-order peak structures, what other phenomena can be caused by spectral interference of high harmonics from subsystems?

In this work, the disorder-induced interference of the HHG spectrum is studied in the Su-Schrieffer-Heeger (SSH) model, which is a simple one-dimensional (1D) tight-binding model with two sites per unit cell and is suitable for polyacetylene polymer chains, carbon nanotubes, perovskites, and so on. [29–32]. Considering that the connections between atoms in a unit cell are more stable than those in adjacent unit cells, we introduce disorder into the atomic spacings between adjacent cells, while the atomic spacings within the unit cells remain fixed [see Fig. 1(a)]. The size of the atomic spacing determines the amplitude of the hopping term. We find that the harmonic spectrum interference between the disordered SSH chains leads to the emergence of a second plateau even though disordered SSH chains are a two-band model. This phenomenon is different from that of the second plateau origin in crystalline materials, which is associated with higher conduction bands [33–36].

This paper is organized as follows. In Sec. II, we present the theoretical model and basic equations. The results are reported and discussed in Sec. III, and a brief conclusion is presented in Sec. IV. Atomic units (a.u.) are always used unless otherwise specified.

*xuebin.bian@wipm.ac.cn

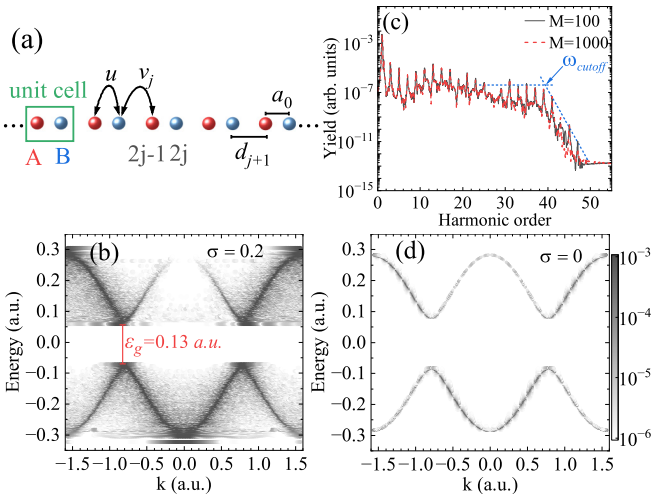

FIG. 1. (a) Schematics of the periodic boundary SSH model with disordered intercell hopping terms. Atoms A and B constitute a unit cell and u (v_j) is the intracell (intercell) hopping term. a_0 and d_j denote, respectively, the intracell atomic spacing and the adjacent intercell atomic spacing. The value of hopping terms are determined by the atomic spacing [see Eqs. (2) and (3)]. Band structures for (b) the disordered ($\sigma = 0.2$) system and (d) the ordered ($\sigma = 0$) system are obtained by transforming the real-space eigenstates to k-space using Fourier transformation. (c) HHG spectra from 100 and 1000 configurations, respectively. The dotted straight lines are guides to the eye for identifying the spectral cutoff.

II. THEORETICAL METHOD

We consider the following one-dimensional (1D) periodic boundary dimerized chain with disordered intercell hopping as shown in Fig. 1(a)

$$\hat{H}_0 = \sum_{j=1}^{N} (u\,|2j-1\rangle\langle 2j| + v_j\,|2j\rangle\langle 2j+1| + \text{H.c.}), \quad (1)$$

where atoms $2j-1$ and $2j$ form a unit cell and the integer j labels the atomic sites. u and v_j are the intracell and intercell hopping terms, respectively. We assume an exponential dependence of tunneling probability between neighboring sites on distance, and set the hopping terms as [37]

$$u = -\exp[-(x_{2j} - x_{2j-1})] = -\exp(-a_0), \quad (2)$$

$$v_j = -\exp[-(x_{2j+1} - x_{2j})] = -\exp(-d_j), \quad (3)$$

where a_0 denotes the atomic spacing within the unit cell and is kept constant. The spacing d_j between atoms $2j$ and $2j+1$ from adjacent unit cells follows a truncated normal distribution with an average spacing d_0. In this model, we choose $a_0 + d_0 = 4$ a.u. and $a_0 = 1.7$ a.u. However, our findings are not contingent upon specific parameters within the model.

Figure 1(b) shows an example of the band structure of the disordered SSH chain for the number of unit cell $N = 4096$ and the statistical fluctuation $\sigma = 0.2$. The band structure of the ordered ($\sigma = 0$) SSH chain is presented in Fig. 1(d) for comparison. As we can see, both ordered and disordered SSH chains exhibit two distinct energy band segments (valence and conduction bands). The minimal and maximal band gaps for the disordered SSH chain are $\varepsilon_g = 0.13$ a.u. and $\varepsilon_m = 0.62$ a.u., respectively.

The coupling between the chain and an external field is described in the velocity gauge, and then the time-dependent Hamiltonian can be written as

$$\hat{H}(t) = \sum_{j=1}^{N} [u(t)\,|2j-1\rangle\langle 2j| + v_j(t)\,|2j\rangle\langle 2j+1| + \text{H.c.}], \quad (4)$$

where the time-dependent hopping terms are

$$u(t) = u\exp[-iA(t)a_0], \quad (5)$$

$$v_j(t) = v_j\exp[-iA(t)d_j]. \quad (6)$$

$A(t) = -\int_{-\infty}^{t} F(\tau)\mathrm{d}\tau$ is the vector potential and the electric field $F(t) = F_0\cos(\omega_0 t)f(t)$. The envelope function $f(t)$ is trapezoidal with five cycles at peak intensity (3-5-3). In the simulation of HHG, we employ the first N eigenstates of field-free Hamiltonian as initial states and the time-dependent wave functions $|\psi_n(t)\rangle = \sum_j a_j(t)\,|j\rangle$ can be obtained by solving Eq. (4) using the fourth-order Runge-Kutta method. The current operator can be represented as

$$\hat{j}(t) = i\sum_{j=1}^{2N} r_j h_j(t)\,|j\rangle\langle j+1| - \text{H.c.}, \quad (7)$$

where r_j and $h_j(t)$ represent the distance and time-dependent hopping terms between atoms j and $j+1$. Thus the current for the chain reads

$$J(t) = \sum_n \langle\psi_n(t)|\,\hat{j}(t)\,|\psi_n(t)\rangle\,, \quad (8)$$

and the HHG spectrum can be obtained by squaring the absolute value of the Fourier-transformed current.

Compared to the previous work using a uniformly distributed disorder in short chains with one type of atoms [38], the disordered SSH long chain we consider involves each unit cell having two types of atoms, with the intercell distances following a truncated normal distribution. Additionally, compared to the complex plateau structure shown in Ref. [38] attributed to a model involving multiple bands, the harmonic spectra of the two-band disordered SSH model exhibit a simpler and cleaner plateau structure, facilitating our analysis of its origin. To enable computational implementation, we followed the approach outlined in Ref. [28], which has also been employed for simulating the liquid HHG [24,39] and liquid terahetz wave generation [40]. According to this approach, the HHG spectrum of the disordered SSH long chain can be obtained by decomposing the long chain into M short chains, each consisting of $2N = 512$ atoms, and coherently superimposing the Fourier-transformed currents from these short chains. In this case, the total HHG spectrum can be written as

$$I(\omega) = \left|\frac{1}{M}\sum_{m}^{M}\mathcal{F}[J_m(t)]\right|^2, \quad (9)$$

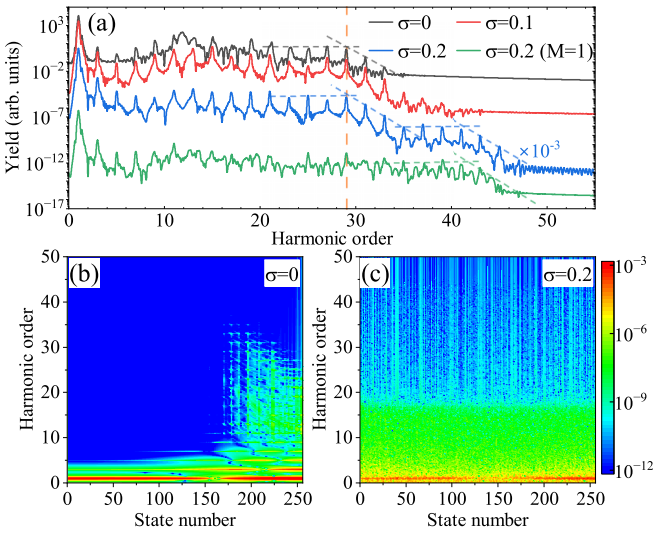

FIG. 2. (a) HHG spectra for the ordered and disordered SSH chains. From top to bottom, the statistical fluctuation σ is 0, 0.1, 0.2, and 0.2 ($M = 1$). (b) HHG spectra corresponding to each initial state in the ordered SSH chain. (c) Same as (b) but using $\sigma = 0.2$ (disorder). The peak of laser intensity is 0.4 TW/cm^2. Dashed straight lines are guides to the eye.

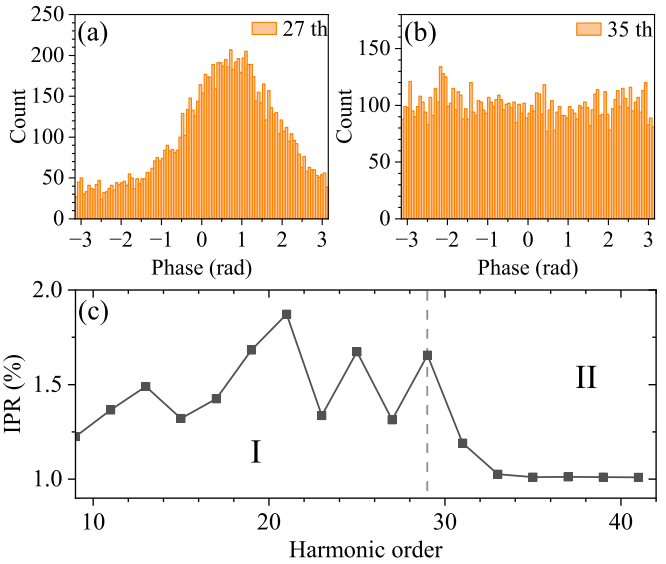

FIG. 3. Histogram of the phase of (a) the 27th-order harmonic and (b) 35th-order harmonic. (c) IPR of the harmonic phase versus harmonic order for the system with $\sigma = 0.2$, $I_0 = 0.4$ TW/cm^2, and $\lambda = 3200$ nm. The dashed line in (c) corresponds to the cutoff energy of the first plateau in HHG spectrum.

where the subscript m denotes the mth atomic chain. Each short chain with the same statistical distribution can be considered as a distinct region of the disordered SSH long chain. Here, we focus on the multiplateau structure of the HHG spectrum caused by spectra interference from different regions of the disordered long chain. Figure 1(c) shows the HHG spectra for $\sigma = 0.2$ when $I_0 = 1$ TW/cm^2 and laser wavelength $\lambda = 3200$ nm. We notice that the harmonic spectrum has converged when $M = 100$ is employed. To further ensure the convergence of harmonic spectra under the parameters utilized in this work and to facilitate the analysis of interference in harmonic spectra among different subsystems in subsequent sections, $M = 10^4$ is adopted unless otherwise stated.

III. RESULT AND DISCUSSIONS

In this section, we first show the multiplateau structure of the HHG spectrum induced by disorder in SSH chains and analyze the interference of harmonic spectra between disordered atomic chains. Then, we present the range of laser intensities for the appearance of the multiplateau structure. In these calculations, the laser wavelength is fixed at $\lambda = 3200$ nm.

A. Multiple plateau structure

In Fig. 2(a), we show the averaged HHG spectra for different σ at a laser intensity of 0.4 TW/cm^2. The black dashed line indicates the spectral cutoff of the ordered SSH chain. It can be seen that with the increase of σ, the yield in the plateau region of the HHG spectrum decreases, and at the same time, the peak structures become cleaner.

For comparison, we show the HHG spectrum of a single disordered ($\sigma = 0.2$) SSH chain in Fig. 2(a) with a green line. The harmonic spectra resulting from each initial state of the ordered and a single disordered SSH chains are shown in Figs. 2(b) and 2(c), respectively. For the ordered chain, the harmonic spectrum near the top of the valence band dominates the total harmonic spectrum. This is attributed to the fact that, in periodic systems, electron-hole pairs are born mainly at the minimum band gap, and the motion of electron-hole pairs in reciprocal space satisfies the acceleration theorem [10,41]. However, for the disordered SSH chain, the introduction of disorder breaks the periodicity of the system, causing the acceleration theorem to fail. In this case, electrons at the bottom of the valence band can be resonantly excited to the top [42], so we can see in Fig. 2(c) that the harmonic spectra corresponding to all initial states of the disordered SSH chain contribute to the total HHG spectrum. This results in the spectral cutoff of the disordered SSH chain being higher than that of the ordered chain under the same driving field.

It is noteworthy that by using Eq. (9) to average the harmonic spectra of $M = 10^4$ disordered chains, a double-plateau structure appears in the resultant harmonic spectrum [see the blue line in Fig. 2(a)]. The spectral cutoff of the first plateau is the same as that of the ordered SSH chain, while the second plateau is consistent with that of a single disordered SSH chain (about $41\omega_0$). We attribute the formation of the double-plateau structure to the coherent superposition of harmonic spectra from multiple disordered chains. To verify this, we proceed to analyze the harmonic phase of each individual disordered chain.

The statistical distributions of the harmonic phases φ for orders 27 and 35 are presented in Figs. 3(a) and 3(b), respectively. These two order harmonics are located at the first and second spectral plateaus, respectively. As we can see, the statistical distribution of the 27th-order harmonic phase D_{27} exhibits a clear unimodal structure with the harmonic phase being mainly localized around $\varphi = 0.8$ rad. However, for the

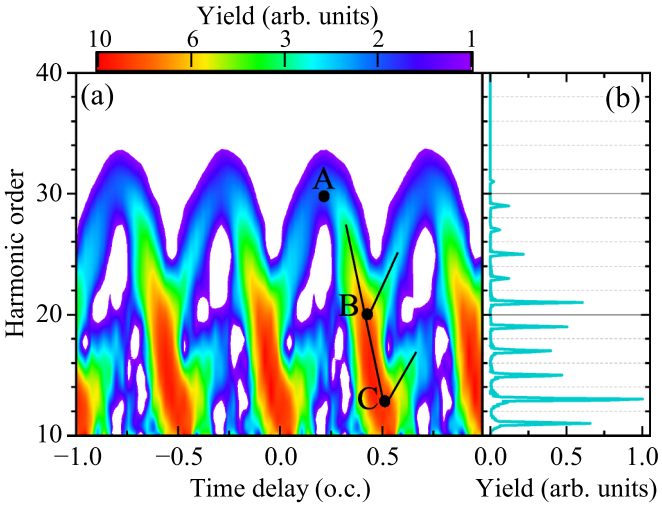

FIG. 4. (a) Time-frequency analysis, with a 0.3 cycles wide Blackman window, for laser intensity $I_0 = 0.4$ TW/cm^2. (b) Normalized HHG spectrum of (a). Points A, B, and C in (a) correspond to the locations of multiorbital coalescence.

35th-order harmonic, the phase distribution is more uniform with only a weak peak at $\varphi = -2.2$ rad. In general, for a more localized distribution of D_n, the interference enhancement between harmonics from different chains is stronger and vice versa. The degree of localization of the phase distribution is quantified by the inverse participation ratio (IPR)

$$\mathrm{IPR}(n) = \left[\sum_{l}^{L} D_n^2(l)\right] \Big/ \left[\sum_{l}^{L} D_n(l)\right]^2, \qquad (10)$$

where $D_n(l)$ denotes the count of atomic chains whose phase falls into interval $(2(l-1)\pi/L, 2l\pi/L]$ for the nth order harmonic. A higher IPR means stronger localization. In Fig. 3(c), we show the IPR spectrum and divide it into two parts according to the first harmonic plateau cutoff (see the black dashed line). These two parts correspond to the two harmonic plateaus. It can be found that the IPR in the first plateau region is significantly larger than that in the second plateau region, which is the reason for the formation of the second HHG plateau.

One can notice in Fig. 3(c) that the first plateau has four distinct peak structures at orders of 13, 21, 25, and 29, which implies that the harmonic yield corresponding to these peaks is higher than those of the neighboring orders. In the following, we discuss the origin of the peak structure at orders of 13, 21, and 29, while the origin of the peak structure at the 25th order has not been found. For this purpose, we show the HHG spectrum of the disordered system from Fig. 3(a) again in Fig. 4(b) after normalizing it and using a linear scale. It is obvious that the harmonic yield corresponding to the peak of the IPR spectrum is higher than those of neighboring orders. For further analysis, the time-frequency structure of HHG is shown in Fig. 4(a) using a 0.3 cycle Blackman window scanned across two optical cycles near the peak of

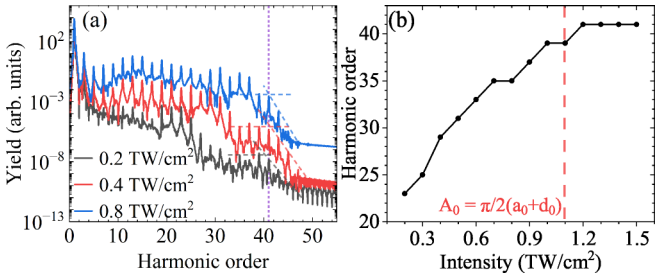

FIG. 5. (a) HHG spectra for $I_0 = 0.2$ TW/cm^2 [black line (lower)], $I_0 = 0.4$ TW/cm^2 [red line (middle)], and $I_0 = 0.8$ TW/cm^2 [blue line (upper)]. (b) The dependence of the first plateau cutoff in the HHG spectrum on laser intensity. $\sigma = 0.2$ is adopted here. Dashed straight lines are guides to the eye.

the pulse. The relationship between the harmonic energy ω and the radiation time t_r shows an inverted-F structure in a half cycle [see the black line in Fig. 4(a)]. Points B and C are the crossing points of the inverted-F. Point A corresponds to $\mathrm{d}\omega/\mathrm{d}t_r = 0$. This means that two or more HHG radiation orbits coalesce at these three points, leading to the caustics enhancement in the HHG spectrum [43–46]. Therefore, the phase distribution of the caustic point in the HHG spectrum is more localized compared with its neighboring orders.

B. Laser intensity dependence

To illustrate the dependence of the disorder-induced double-plateau structure on laser parameters, we present HHG spectra at various laser intensities in Fig. 5(a). As the laser intensity increases, the first HHG plateau cutoff rises while the spectral cutoff of the second plateau is fixed at 41st order [see the purple dotted line in Fig. 5(a)], approaching the maximum band gap. In other words, when the spectral cutoff of the first HHG plateau is below the maximum band gap, the harmonic spectrum of the disordered SSH chains exhibits a double-plateau structure. The dependence of the first plateau cutoff on laser intensity is shown in Fig. 5(b). The first plateau cutoff reaches its maximum value at a laser intensity of 1.2 TW/cm^2 and no longer changes with increasing laser intensity. At this laser intensity, the vector potential corresponds to about $\pi/2(a_0 + d_0)$ [see the red dashed line in Fig. 5(b)].

IV. CONCLUSION

We conducted a numerical investigation into the spectral interference of HHG within the disordered SSH systems. Compared with the ordered SSH chain, the HHG spectrum of a single disordered SSH chain has higher spectral cutoff. After coherently superimposing the harmonic spectra from a sufficient number of disordered SSH chains with the same statistical distribution, the averaged harmonic spectrum exhibits a double-plateau structure. The first plateau in the averaged HHG spectrum has the same cutoff as that of the ordered SSH chain, and the second plateau cutoff is close to the maximum band gap. Statistical analysis of the harmonic phases from 10^4 disordered SSH chains indicates that the double-plateau structure in the disordered SSH chain results

from the spectral interference between different regions. Furthermore, we find that the phase distribution at the caustic point of the HHG spectrum is more localized compared with the neighboring orders, where the spectral caustic point can be confirmed by time-frequency analysis of the harmonic spectrum.

ACKNOWLEDGMENTS

This work is supported by the National Natural Science Foundation of China (Grant No. 12247122) and the CAS Project for Young Scientists in Basic Research (Grant No. YSBR-059).

[1] M. Hentschel, R. Kienberger, C. Spielmann, G. A. Reider, N. Milosevic, T. Brabec, P. Corkum, U. Heinzmann, M. Drescher, and F. Krausz, Attosecond metrology, Nature (London) **414**, 509 (2001).

[2] P. M. Paul, E. S. Toma, P. Breger, G. Mullot, F. Augeé, P. Balcou, H. G. Muller, and P. Agostini, Observation of a train of attosecond pulses from high harmonic generation, Science **292**, 1689 (2001).

[3] M. Drescher, M. Hentschel, R. Kienberger, G. Tempea, C. Spielmann, G. A. Reider, P. B. Corkum, and F. Krausz, X-ray pulses approaching the attosecond frontier, Science **291**, 1923 (2001).

[4] J. L. Krause, K. J. Schafer, and K. C. Kulander, High-order harmonic generation from atoms and ions in the high intensity regime, Phys. Rev. Lett. **68**, 3535 (1992).

[5] K. J. Schafer, B. Yang, L. F. DiMauro, and K. C. Kulander, Above threshold ionization beyond the high harmonic cutoff, Phys. Rev. Lett. **70**, 1599 (1993).

[6] S. Ghimire, A. D. DiChiara, E. Sistrunk, P. Agostini, L. F. DiMauro, and D. A. Reis, Observation of high-order harmonic generation in a bulk crystal, Nat. Phys. **7**, 138 (2011).

[7] A. H. Chin, O. G. Calderón, and J. Kono, Extreme midinfrared nonlinear optics in semiconductors, Phys. Rev. Lett. **86**, 3292 (2001).

[8] P. B. Corkum, Plasma perspective on strong field multiphoton ionization, Phys. Rev. Lett. **71**, 1994 (1993).

[9] M. Lewenstein, P. Balcou, M. Y. Ivanov, A. L'Huillier, and P. B. Corkum, Theory of high-harmonic generation by low-frequency laser fields, Phys. Rev. A **49**, 2117 (1994).

[10] G. Vampa, C. R. McDonald, G. Orlando, D. D. Klug, P. B. Corkum, and T. Brabec, Theoretical analysis of high-harmonic generation in solids, Phys. Rev. Lett. **113**, 073901 (2014).

[11] T. Higuchi, M. I. Stockman, and P. Hommelhoff, Strong-field perspective on high-harmonic radiation from bulk solids, Phys. Rev. Lett. **113**, 213901 (2014).

[12] E. N. Osika, A. Chacón, L. Ortmann, N. Suárez, J. A. Pérez-Hernández, B. Szafran, M. F. Ciappina, F. Sols, A. S. Landsman, and M. Lewenstein, Wannier-Bloch approach to localization in high-harmonics generation in solids, Phys. Rev. X **7**, 021017 (2017).

[13] S. Fu, Y. Feng, J. Li, S. Yue, X. Zhang, B. Hu, and H. Du, Recollision dynamics analysis of high-order harmonic generation in solids, Phys. Rev. A **101**, 023402 (2020).

[14] A. M. Parks, G. Ernotte, A. Thorpe, C. R. McDonald, P. B. Corkum, M. Taucer, and T. Brabec, Wannier quasi-classical approach to high harmonic generation in semiconductors, Optica **7**, 1764 (2020).

[15] Y. Peng, T. Wu, G. Yuan, L. Chi, S. Jiang, K. Dorfman, C. Yu, and R. Lu, Solid state–like high harmonic generation from cluster molecules with rotational periodicities, Sci. Adv. **9**, eadd6810 (2023).

[16] G. Vampa, T. J. Hammond, N. Thiré, B. E. Schmidt, F. Légaré, C. R. McDonald, T. Brabec, D. D. Klug, and P. B. Corkum, All-optical reconstruction of crystal band structure, Phys. Rev. Lett. **115**, 193603 (2015).

[17] L. Li, P. Lan, L. He, W. Cao, Q. Zhang, and P. Lu, Determination of electron band structure using temporal interferometry, Phys. Rev. Lett. **124**, 157403 (2020).

[18] J. Chen, Q. Xia, and L. Fu, Reconstruction of crystal band structure by spectral caustics in high-order harmonic generation, Phys. Rev. A **104**, 063109 (2021).

[19] H. Liu, Y. Li, Y. S. You, S. Ghimire, T. F. Heinz, and D. A. Reis, High-harmonic generation from an atomically thin semiconductor, Nat. Phys. **13**, 262 (2017).

[20] T. T. Luu and H. J. Wörner, Measurement of the Berry curvature of solids using high-harmonic spectroscopy, Nat. Commun. **9**, 916 (2018).

[21] Y. S. You, Y. Yin, Y. Wu, A. Chew, X. Ren, F. Zhuang, S. Gholam-Mirzaei, M. Chini, Z. Chang, and S. Ghimire, High-harmonic generation in amorphous solids, Nat. Commun. **8**, 724 (2017).

[22] T. T. Luu, Z. Yin, A. Jain, T. Gaumnitz, Y. Pertot, J. Ma, and H. J. Wörner, Extreme–ultraviolet high–harmonic generation in liquids, Nat. Commun. **9**, 3723 (2018).

[23] A.-W. Zeng and X.-B. Bian, Impact of statistical fluctuations on high harmonic generation in liquids, Phys. Rev. Lett. **124**, 203901 (2020).

[24] A. Mondal, O. Neufeld, Z. Yin, Z. Nourbakhsh, V. Svoboda, A. Rubio, N. Tancogne-Dejean, and H. J. Wörner, High-harmonic spectroscopy of low-energy electron-scattering dynamics in liquids, Nat. Phys. **19**, 1813 (2023).

[25] Z.-W. Ding, Y.-B. Wang, Z.-L. Li, and X.-B. Bian, High-order harmonic generation in liquids in bicircularly polarized laser fields, Phys. Rev. A **107**, 013503 (2023).

[26] J. X. Chen and X. B. Bian, Theoretical analysis of high-order harmonic generation in liquids by a semiclassical method, Phys. Rev. A **107**, 043111 (2023).

[27] T.-Y. Du and C. Ma, Temperature-induced dephasing in high-order harmonic generation from solids, Phys. Rev. A **105**, 053125 (2022).

[28] C.-L. Xia, J.-Q. Liu, L.-J. Lü, A.-W. Zeng, Z.-L. Li, and X.-B. Bian, Theoretical study of high-order harmonic generation in solutions, J. Phys. B: At., Mol. Opt. Phys. **55**, 045401 (2022).

[29] W. P. Su, J. R. Schrieffer, and A. J. Heeger, Solitons in polyacetylene, Phys. Rev. Lett. **42**, 1698 (1979).

[30] J. Jiang, J. Dong, and D. Y. Xing, Size and helical symmetry effects on the nonlinear optical properties of chiral carbon nanotubes, Phys. Rev. B **59**, 9838 (1999).

[31] V. Perebeinos, J. Tersoff, and P. Avouris, Electron-phonon interaction and transport in semiconducting carbon nanotubes, Phys. Rev. Lett. **94**, 086802 (2005).

[32] K. H. Ahn, T. Lookman, A. Saxena, and A. R. Bishop, Electronic properties of structural twin and antiphase boundaries in materials with strong electron-lattice couplings, Phys. Rev. B **71**, 212102 (2005).

[33] F. H. M. Faisal and J. Z. Kamiński, Generation and control of high harmonics by laser interaction with transmission electrons in a thin crystal, Phys. Rev. A **54**, R1769(R) (1996).

[34] M. Wu, S. Ghimire, D. A. Reis, K. J. Schafer, and M. B. Gaarde, High-harmonic generation from Bloch electrons in solids, Phys. Rev. A **91**, 043839 (2015).

[35] G. Ndabashimiye, S. Ghimire, M. Wu, D. A. Browne, K. J. Schafer, M. B. Gaarde, and D. A. Reis, Solid-state harmonics beyond the atomic limit, Nature (London) **534**, 520 (2016).

[36] T. Ikemachi, Y. Shinohara, T. Sato, J. Yumoto, M. Kuwata-Gonokami, and K. L. Ishikawa, Trajectory analysis of high-order-harmonic generation from periodic crystals, Phys. Rev. A **95**, 043416 (2017).

[37] C. Jürß and D. Bauer, High-harmonic generation in Su-Schrieffer-Heeger chains, Phys. Rev. B **99**, 195428 (2019).

[38] C. Yu, K. K. Hansen, and L. B. Madsen, High-order harmonic generation in imperfect crystals, Phys. Rev. A **99**, 063408 (2019).

[39] Z. Nourbakhsh, O. Neufeld, N. Tancogne-Dejean, and A. Rubio, An ab initio supercell approach for high-harmonic generation in liquids, arXiv:2212.04177.

[40] Z.-L. Li and X.-B. Bian, Terahertz radiation induced by shift currents in liquids, Proc. Natl. Acad. Sci. **121**, e2315297121 (2024).

[41] F. Rossi and T. Kuhn, Theory of ultrafast phenomena in photoexcited semiconductors, Rev. Mod. Phys. **74**, 895 (2002).

[42] C. L. Xia, Z. L. Li, J. Q. Liu, A. W. Zeng, L. J. Lü, and X. B. Bian, Role of charge-resonance states in liquid high-order harmonic generation, Phys. Rev. A **105**, 013115 (2022).

[43] O. Raz, O. Pedatzur, B. D. Bruner, and N. Dudovich, Spectral caustics in attosecond science, Nat. Photonics **6**, 170 (2012).

[44] D. Faccialà, S. Pabst, B. D. Bruner, A. G. Ciriolo, S. De Silvestri, M. Devetta, M. Negro, H. Soifer, S. Stagira, N. Dudovich, and C. Vozzi, Probe of multielectron dynamics in Xenon by caustics in high-order harmonic generation, Phys. Rev. Lett. **117**, 093902 (2016).

[45] A. J. Uzan, G. Orenstein, Á. Jiménez-Galán, C. McDonald, R. E. F. Silva, B. D. Bruner, N. D. Klimkin, V. Blanchet, T. Arusi-Parpar, M. Krüger, A. N. Rubtsov, O. Smirnova, M. Ivanov, B. Yan, T. Brabec, and N. Dudovich, Attosecond spectral singularities in solid-state high-harmonic generation, Nat. Photon. **14**, 183 (2020).

[46] J. Chen, Q. Xia, and L. Fu, Spectral caustics of high-order harmonics in one-dimensional periodic crystals, Opt. Lett. **46**, 2248 (2021).